Journal of Marine Science and Technology

Volume 26 | Issue 2 Article 7

NON-PREMIXED TRANSVERSELY OSCILLATING PLANE JET FLAMES IN CO-FLOWING AIR STREAMS

Reuben Mwanza Kivindu
Department of Mechanical Engineering, National Taiwan University of Science and Technology, Taipei 10672, Taiwan, Republic of China

Rong Fung Huang
Department of Mechanical Engineering, National Taiwan University of Science and Technology, Taipei 10672, Taiwan, Republic of China., rfhuang@mail.ntust.edu.tw

Ching Min Hsu
Department of Mechanical Design Engineering, National Formosa University, Yunlin County 63246, Taiwan, Republic of China.

Recommended Citation

Kivindu, Reuben Mwanza; Huang, Rong Fung; and Hsu, Ching Min (2018) "NON-PREMIXED TRANSVERSELY OSCILLATING PLANE JET FLAMES IN CO-FLOWING AIR STREAMS," *Journal of Marine Science and Technology*: Vol. 26: Iss. 2, Article 7.
DOI: 10.6119/JMST.2018.04_(2).0007
Available at: https://jmstt.ntou.edu.tw/journal/vol26/iss2/7

Journal of Marine Science and Technology, Vol. 26, No. 2, pp. 194-206 (2018)
DOI: 10.6119/JMST.2018.04_(2).0007

NON-PREMIXED TRANSVERSELY OSCILLATING PLANE JET FLAMES IN CO-FLOWING AIR STREAMS

Reuben Mwanza Kivindu[1], Rong Fung Huang[1], and Ching Min Hsu[2]

Key words: oscillating jet flame, fluidic-oscillator, flame behavior, co-flowing air.

ABSTRACT

This study examined the flame behavior and thermal structure of non-premixed transversely oscillating plane jet flames. A V-shaped fluidic oscillator was installed with deflection plates to merge alternately issued pulsating jets, and induce transverse oscillations of the merged jet. Co-flowing air streams were supplied with two planar air jets arranged next to the burner. Isothermal jet frequencies were detected using single hot-wire anemometry. Flame behaviors were studied using photographic techniques. Flame temperatures were measured using a fine-wire type-R thermocouple, and combustion concentrations of products were measured using a gas analyzer. The Strouhal number for the transversely oscillating jet shows an asymptotic value of 0.188. Three flame modes exist in the domain of the jet Reynolds number Re and the co-flow air Reynolds number Re_a: attached flame, transitional flame, and lifted flame. At $Re < 1204$, the axial location of the maximum flame width decreases as Re_a increases, while at $Re > 1204$, the axial location of the maximum flame width increases as Re_a increases. As Re_a increases, the flames become thinner, the maximum flame width decreases, and the maximum flame temperature increases. Co-flow air Re_a of 846 produces higher flame temperatures by approximately 100°C compared with the co-flow air Re_a of 445. The analysis reveals that high velocity co-flow air results in better combustion performance when compared to low velocity co-flowing air. The combustion characteristics of the transversely oscillating plane jet flames improved significantly, especially with high velocity co-flow air due to the enhanced jet turbulence, entrainment, and mixing.

Paper submitted 08/30/17; revised 12/15/17; accepted 01/05/18. Author for correspondence: Rong Fung Huang (e-mail address: rfhuang@mail.ntust.edu.tw).
[1] Department of Mechanical Engineering, National Taiwan University of Science and Technology, Taipei 10672, Taiwan, Republic of China.
[2] Department of Mechanical Design Engineering, National Formosa University, Yunlin County 63246, Taiwan, Republic of China.

I. INTRODUCTION

The research involving fluidic oscillators has intensified experimentally and numerically over the past few decades (Gebhard et al., 1996; Uzol and Camci, 2002; Chang and Huang, 2004; Huang and Chang, 2005; Chen et al., 2006; Huang and Chang, 2007; Yang et al., 2007b; Mack et al., 2011). This is due to their simplicity and wide scope of applications in areas such as combustion, heat transfer, mixing processes, flow actuators, and flow meters (Gregory et al., 2007; Yang et al., 2007a; Sun and Sun, 2011; Tesař et al., 2013; Raghu, 2013; Rasheed, 2013). In its simplest form, a fluidic oscillator is a device that utilizes the Coanda effect to induce self-sustained jet oscillations when supplied with a steady fluid flow. When a fluid jet is injected into the oscillation chamber, it bends towards one of the walls due to flow instability. This develops a pressure gradient across the jet and in the trapped bubble, which is responsible for the jet oscillation inside the chamber (Joyce, 1983; Gebhard et al., 1996; Olivotto, 2010; Del Campo et al., 2015). Fluidic oscillators have no moving parts, are reliable and less expensive, and have no maintenance requirements (Tesař et al., 2013).

Other studies have identified the main geometric factors that influence the performance of fluidic oscillators. For microfluidic oscillators, a large aspect ratio (*AR*) nozzle lessens the domination of viscous force in the micro-channel thus promoting the Coanda effect (Yang et al., 2007a). The inlet length before the nozzle exit has no effect on the performance of the fluidic oscillator (Mack et al., 2011; Tesař et al., 2014). The oscillation frequency increases as the aspect ratio increases (Shakouchi, 1989). Numerical investigations on fluidic micro-oscillators show that characteristic parameters, such as frequency, volumetric flow rate, and output pressure depend strongly on the nozzle geometry (Gebhard et al., 1996). The interaction, size change, and blockage effect of the trapped vortex pair in the oscillatory chamber are the main driving mechanisms of the jet oscillation (Uzol and Camci, 2002; Huang and Chang, 2005; Mataoui and Schiestel, 2009). The optimization of geometric factors has improved the performance of fluidic oscillators, thus enabling their applications in combustion and mixing operations.

The variation in the pressure gradient across the jet and at the vortex centers due to the varying size of the counter-rotating

vortex pair keeps the jet oscillating back and forth inside the oscillation chamber (Chen et al., 2006; Huang and Chang, 2007; Sun and Sun, 2011). This allows the fluidic oscillator to enhance entrainment and mixing. Since jet oscillation properties are dependent on the Reynolds number, so are Stouhal number and the amplitude of oscillations (Boucher and Mazharoglu, 1988; Gebhard et al., 1996). The Strouhal number affects the entire field that is generated by the precessing jet. The occurrence of a precessing jet promotes the interaction between the jet and the ambient fluids, thereby increasing large-scale entrainment and mixing, whereas the fine-scale turbulent mixing is suppressed (Mi and Nathan, 2005). Therefore, the fluctuation intensity, decay rate, and half-width of the precessing jet velocity field significantly increase in the near field as the Strouhal number increases.

Experimental and computational visualization of jet oscillations inside a fluidic oscillator shows that the concavity of the oscillation chamber wall and its location from the jet exit plane is an important factor for maintaining the jet oscillation. This study showed that running at low Reynolds numbers results in low oscillation frequencies: the investigators obtained a maximum frequency of approximately 15 Hz (Uzol and Camci, 2002). The large size that results from the inclusion of the concave targets, and the low oscillation frequencies makes fluidic oscillators suitable for applications in industrial burners. This is because they provide stable flames and reduce pollutant emissions.

A crescent-surface target blockage was inserted into the downstream cavity of a slit V-gutter to develop a V-shaped fluidic oscillator (Huang and Chang, 2005). The fluidic oscillator produced jets of stable, self-sustained, and periodic oscillations in the near-wake region when compared to the closed-tip V-gutter. Huang and Chang (2007) developed a fluidic oscillator to investigate the evolution process and turbulence properties of a transversely oscillating flow in a gravity-driven water tunnel. Two short deflection plates installed at the exits of a fluidic oscillator merge the issued pulsating jets and form a counter-rotating vortex pair in the near-wake region of the oscillator. The stagnation point of the counter-rotating vortex pair moves back and forth, thereby creating a transversely oscillating flow downstream of the impingement. The integral time and length scales of the turbulence eddies produced by the oscillating flow are drastically reduced. Thus, the developed fluidic oscillator appears to be suitable for situations requiring large mass, momentum, and energy dispersion over a short distance.

A jet-impingement fluidic oscillator with a pulsation Strouhal number with an asymptotic value of approximately 0.0029 was used to investigate the flame behavior and thermal structure of a pulsating plane jet flame (Huang et al., 2012). Pulsating plane jet flames show better combustion performances when compared to non-pulsating plane jet flames. Lifted fluidic-oscillator flames exhibit partially premixed flame characteristics unlike plane jet flames (Yang et al., 2014a). Yang et al. (2014b) examined a V-shaped bluff-body burner in order to understand the flame behaviors of bifurcated jets. The bifurcated jet flames have three modes: attached flame, transitional flame, and lifted flame. The improved performance characteristics of pulsating plane jet and bifurcated jet flames are as a result of enhanced entrainment, mixing, and modification of the conventional plane jet. Thus, fluidic oscillators can improve the combustion performances of plane jets.

Studies on lifted flame behavior and co-flowing air show that the height of flame liftoff increases with the velocity of the jet exit and as co-flowing air velocity increases (Montgomery et al., 1998; Akbarzadeh and Birouk, 2014). For high-velocity co-flowing air, the inner shear -layer vortices form farther downstream and the jet spreads more slowly, which moves the flame stabilization farther downstream (Brown et al., 1999; Akbarzadeh and Birouk, 2014). At a certain jet velocity, increasing the co-flow air velocity results in a thinner flame and higher maximum flame temperature. At a low relative velocity of the co-flow air and fuel, the mixing process slows, resulting in smaller flame length, wider flame, and lower flame temperature that extends into a larger area (Namazian, 2016). Therefore, the supply of co-flowing air to transversely oscillating fuel jets may enhance combustion performance because it is possible to manipulate the shear-layer vortical structures to improve entrainment and mixing.

This study installs deflection plates to a V-shaped fluidic-oscillator in order to induce transverse oscillations in a fuel jet that emerges in an environment of co-flowing air streams. The induced transverse oscillations are studied using isothermal flow conditions. The flame behaviors and thermal structures of the transversely oscillating jet flames are studied by varying the fuel jet flow velocity at various co-flow air velocities. The results of this study are analyzed and discussed in this paper.

II. EXPERIMENTAL METHODS

1. Burner Configurations

This study develops and uses a V-shaped fluidic-oscillator burner with installed deflection plates in order to induce transverse oscillations to a plane jet, as shown in Fig. 1 (Huang and Chang, 2007). Two rectangular channels stood along the sides of the burner to provide co-flowing air. The oscillation cavity was made up of an assembly of two blocks configured into a Y-shape and a target blockage with a crescent surface. The target blockage had a downstream width of w_b = 15 mm, and a crescent surface radius of R = 4.5 mm with its center offset from the Y-shape configuration virtual point with a height h = 2 mm. The flow entered the oscillator cavity through a rectangular channel with a width of d = 1 mm, and exited through two passages with widths of b = 0.5 mm that were formed between the Y-shaped configured plates and the target blockage. Deflection plates with lengths of l = 5.5 mm were installed near the fluidic-oscillator exit slots at an angle of θ= 60º from vertical with the plates top tips at a distance of d_p = 11 mm apart. The width of the oscillator was w = 21 mm. The rectangular channels for the co-flow air were D = 5.5 mm in width and made of a plate with a thickness of b_t = 2 mm. The span length of the burner

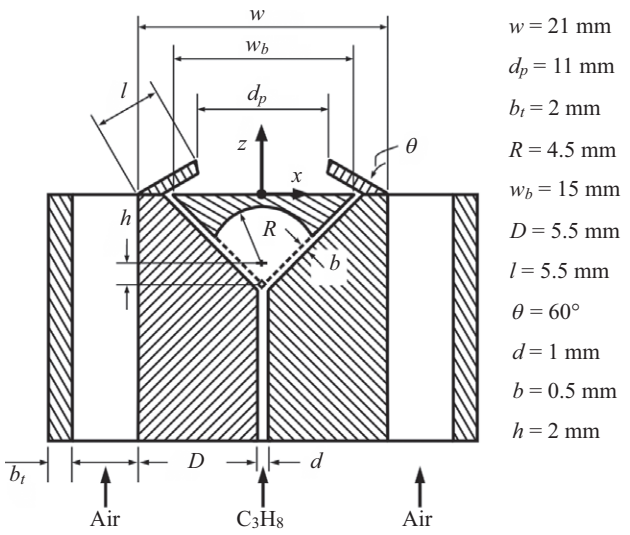

Fig. 1. Experimental setup.

was s = 36 mm. The aspect ratio (AR) for the burner and the co-flow ducts were 36 (s/d) and 6.55 (s/D), respectively. Hence, the flow before being injected into the fluidic-oscillator cavity was considered statistically two-dimensional (Deo et al., 2007). All the burner components described above were made of stainless steel materials. The fluid passed through a rectangular channel containing a set of flow-conditioning honeycombs and screens, a nozzle with a fifth-power polynomial profile, and finally, a 1 mm rectangular channel that injected the flow into the fluidic-oscillator cavity. Pressure regulators, needle valves, and rotameters installed in the piping systems controlled the flow. The rotameters were calibrated using a micro-pressure calibration system composed of an electronic high-precision pressure transducer that was connected to a pitot tube installed in the test section of a wind tunnel. The fuel gas was supplied from a propane pressure tank containing commercial grade propane (95.0% C_3H_8, 3.5% C_2H_6, and 1.5% C_4H_{10}). The co-flow air was tapped from a compressed air system installed in the laboratory and passed through a silica gel filter and then into a flow conditioner composed of honeycombs and screens before being delivered to the co-flow ducts. The fuel jet Reynolds number was defined as $Re = u_j d/\upsilon_c$, where, u_j is the average jet velocity at exit (which was determined by the measured flow-rate Q_c), d is the width of the rectangular channel, and υ_c is the kinematic viscosity of the fuel. The Cartesian coordinate system (x, y, z) used in this experiment was fixed on the downstream surface of the target blockage. The test conditions in this study consisted of varying the fuel jet and co-airflow exit velocities. The experiments were carried using a wire mesh guard when there was minimal activity in the lab in order to avoid influences environmental influences.

2. Jet Oscillation Detection

A constant-temperature, one-component, hot-wire anemometer was used to detect the jet oscillation frequencies and measure the instantaneous jet velocities under isothermal conditions. The hot-wire anemometer calibration was conducted in a wind tunnel using a Pitot tube that was associated with a high-precision pressure transducer. The calibration data was fitted to a fourth-order polynomial to fit the calibration data to null velocity in order to cater to the low velocities that were beyond the lower limit of the Pitot tube (lower limit of the Pitot tube is approximately 0.4 m/s). The output signals from the hot-wire anemometer were analog-filtered using an electric filter to avoid aliasing. The electric filter cut-off frequency was 6 kHz, which was high above the highest expected jet oscillation frequency. The filtered output signals were captured using a data acquisition system and fed into a fast Fourier transform analyzer and a high-speed personal computer for analysis. The hot-wire anemometer was a single TSI 1210-T1.5 hot-wire probe with the original tungsten wire replaced with a platinum wire with a diameter of 5 μm and a length 1.5 mm. The data were logged at a sampling rate of 30,000 samples per second for a duration of three seconds.

3. Flame Visualization

To envisage the flame behavior, both short- and long-exposure images were captured using a digital camera (Nikon Corp., model D3200) with an exposure time range of 1/4,000 - 30 s and a single-lens reflex with an effective view angle of 1.5 × lens focal length. The camera sensor was 23.2 × 15.4 mm CMOS sensor, and a resolution of 6016 × 4000 pixels was used. The flame images were captured with the camera facing in the y-direction. Near-field and instantaneous full-flame images were acquired with a short exposure time of 1 ms. Time-averaged full flame images were acquired with a long exposure time of 2 s. The flame width and length data were attained by averaging approximately 25 and 40 long-exposure images, respectively.

4. Temperature Measurements

The flame temperatures were measured using a homemade fine-wire type-R thermocouple probe. Measurements were taken both transversely and axially to the flame. The probe consisted of a 125 μm diameter wire with a 175 μm diameter spark-welded bead. The sensing bead protruded 10 mm away from the tip of a two-holed ceramic tube stem with a diameter of 2 mm. The ceramic tube was securely fastened in an L-shaped stainless steel tube where a plug was attached in order to ensure the rigidity of the probe. Data were acquired at a sampling frequency of 2 Hz within a fixed period of 4.5 minutes for each measurement point. The probe assembly was positioned in the test section with the aid of a traversing mechanism that had a minimum step resolution of 10 μm. Temperature data acquisition was done using a data logger (Yokogawa Corp., model MX100-E-1D) that was connected to a high-speed personal computer via an Ethernet and processed using MX100 Standard software.

5. Product Concentration Measurements

The product concentrations were measured using a portable

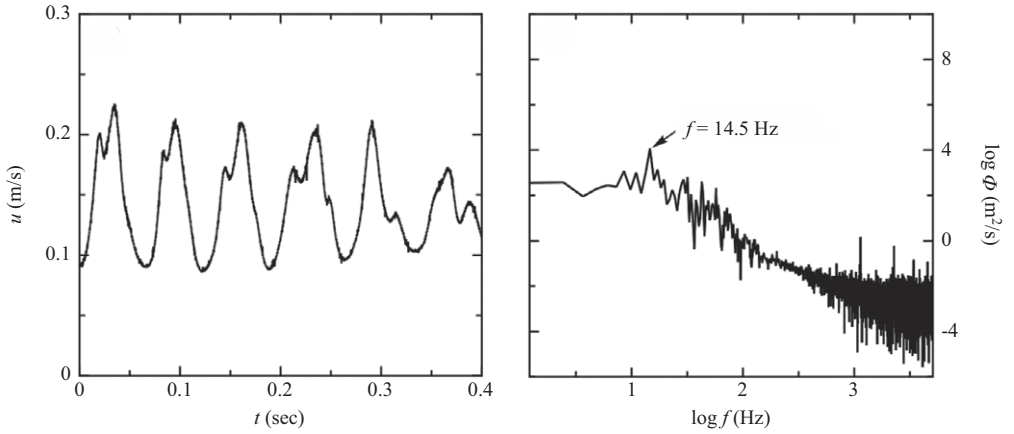

(a) Time histories (b) Power spectrum density function

Fig. 2. Hot-wire anemometer output signals of jet transverse oscillations induced by a V-shaped fluidic-oscillator burner with deflection plates installed at 60° to the vertical. Jet fluid: air, Re = 121. Measured at $(x/d_p, z/d_p) = (0, 0.7)$.

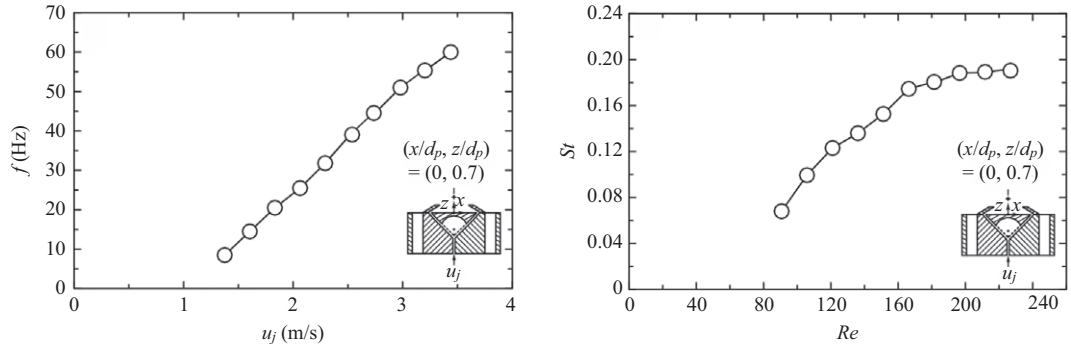

(a) Transverse oscillation frequencies (b) Transverse oscillation Strouhal numbers

Fig. 3. Instabilities induced at exit of V-shaped fluidic-oscillator burner with deflection plates. Jet fluid is air.

multi-gas analyzer (NOVA Inc., Model 7466 K). The gas analyzer simultaneously measured the concentrations of oxygen (O_2), carbon dioxide (CO_2), carbon monoxide (CO), and unburned hydrocarbons (*UHC*). The gas analyzer used the non-dispersive infrared detector to measure the concentrations of CO, CO_2, and UHC, and used a long-life electrochemical sensor to detect the concentrations of O_2. The full-scales measurements for O_2, CO, CO_2, and UHC were 25%, 10%, 20%, and 20%, respectively. The uncertainty was ±1% of full scale. The response time of the gas analyzer was 8-10 s. The probe used for gas sampling was an L-shaped stainless steel tube with an outer diameter of 3 mm and an inner diameter of 2.4 mm. A suction pump drew the gases continuously through the L-shaped suction probe and a dehumidifying system. The gases were then directed into the gas analyzer through a soot remover. A preliminary test identified the suction-flow rate of 850 cm^3/min in order to ensure the least influence on the flow and the flame. Long-term data stabilized within 5 minutes were recorded for each point sampled. The probe assembly was positioned in the test section using a traversing mechanism.

III. RESULTS AND DISCUSSION

1. Jet Oscillations

Figs. 2(a) and (b) show, the instantaneous velocity histories and power spectrum density function Φ of a transversely oscillating jet at Re = 121, respectively. The air jet Reynolds number obtained was, $Re = u_j d_p / \nu_a$. The hot-wire anemometer probe location is $(x/d_p, z/d_p) = (0, 0.7)$. The time series of the instantaneous velocity data was converted into a power-spectrum-density function using the discrete fast Fourier transform technique. In Fig. 2(a), the time series waveform shows clear characteristics of periodic oscillations. Fig. 2(a) shows the corresponding power-spectrum-density function with a unique peak at a frequency of 14.5 Hz, which is interpreted as the periodic oscillation frequency of the jet that was issued from the separation between the tips of the deflection plates. According to Huang and Chang (2007), transverse jet oscillations are induced by the back-and-forth movement of the impingement point, which is formed by the alternative issuing of the jets from the side passages of the fluidic oscillator.

Figs. 3(a) and (b) show the transverse oscillation frequencies and Strouhal numbers, respectively. Measurements were taken at the location $(x/d_p, z/d_p) = (0, 0.7)$. As shown in Fig. 3(a), the oscillation frequency increases almost linearly as the central

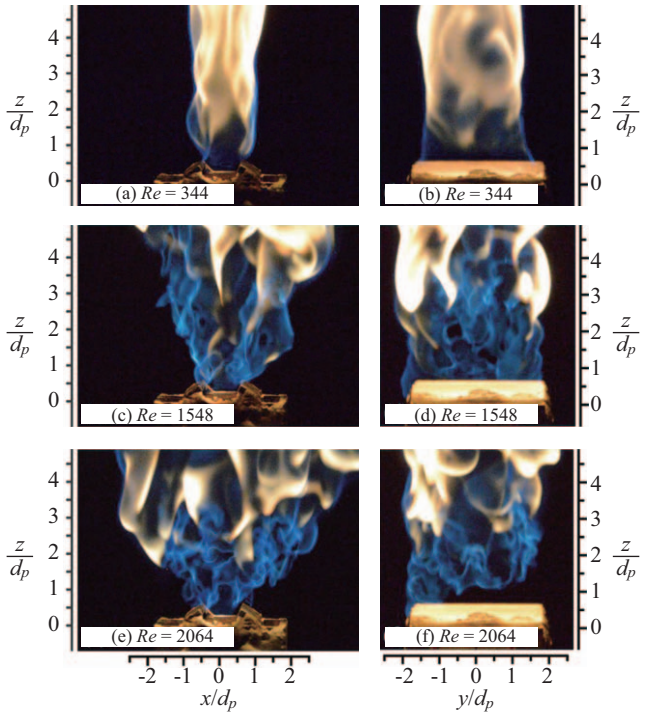

Fig. 4. Typical flame appearances around near exit region of transversely-oscillating jet flames. Re_a = 445. Exposure time 1 ms. (a), (c) and (e) pictures taken with the camera facing *y*-direction. (b), (d) and (f) pictures taken with the camera facing *x*-direction. (a, b) attached flame, (c, d) transitional flame, (e, f) lifted flame.

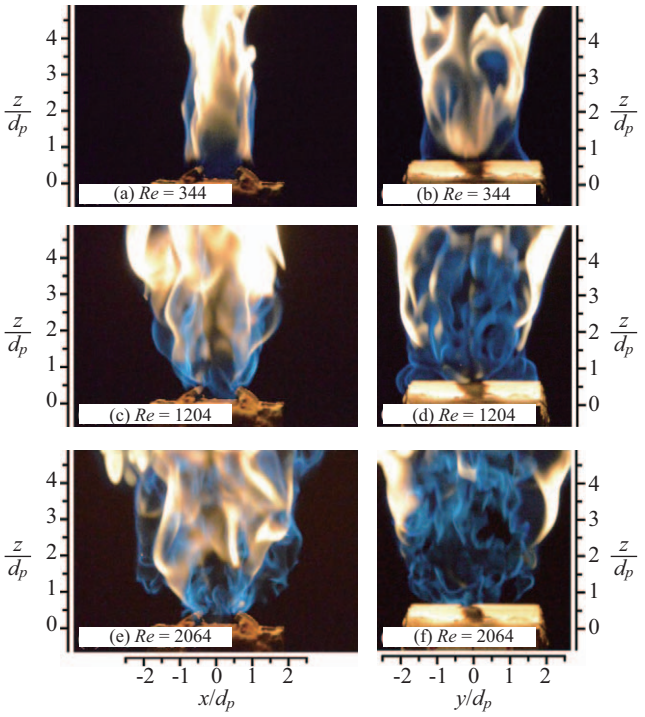

Fig. 5. Typical flame appearances around near exit region of transversely-oscillating jet flames. Re_a = 846. Exposure time 1 ms. (a), (c) and (e) pictures taken with the camera facing *y*-direction. (b), (d) and (f) pictures taken with the camera facing *x*-direction. Attached flame.

jet velocity, u_j, increases. When the u_j value is lower than approximately 1.4 m/s, the jet ceases to oscillate and the flow emerges as a non-oscillating stream. In Fig. 3(b), the Strouhal number, defined as $St = fd_p/u_j$, increases as the Reynolds number increases. The Strouhal number is $St \approx 0.068$ at $Re \approx 90$ and may approach a constant value of $St \approx 0.188$ when Re is greater than approximately 230.

2. Appearances of Flames

Fig. 4 shows typical flame images near the exit of the V-shaped fluidic-oscillator burner with deflection plates at various jet Reynolds numbers. The Reynolds number (Re_a) of the co-flowing air was 445, where $Re_a = u_aD/v_a$, u_a is the volumetric mean velocity of the co-flowing air when exiting the channel, D is the width of the co-flow air channel, and v_a is the kinematic viscosity of the air. The left column images (Figs. 4(a), (c), and (e)) were taken with the camera facing the *y*-direction, while the right column images (Figs. 4(b), (d), and (f)) were taken with the camera facing the *x*-direction. The blue flame zones at the base become lager and wider as Re increases (Figs. 4(a)-(f)). For fixed co-flow air, Re_a, the velocity gradient increases as Re increases, thereby enhancing entrainment and mixing. At a low Reynolds number (Re = 344) (Figs. 4(a) and (b)), two diffusion flames attach to the deflection plates and show a relatively smooth surface. At an axial level of about $z = 1.2\ d_p$ the two blue flames merge to form a single wide yellowish flame, whose surface is wrinkled in a regular manner. Corresponding to Fig. 4(a) is Fig. 4(b) that shows the *x*-direction view of the flame. Fig. 4 (b) show a flame with blue edges and yellowish undisturbed surface. This flame does not show any fluctuations. For Re_a = 445, such flame was observed at the range of Re < 1376. At a mediate jet Reynolds number (Re = 1548) (Figs. 4(c) and (d)), the flame becomes wrinkled and fluctuates rapidly. The mediate flame has a large portion of distributed blue flame at the base. The flame show distorted edges and torn flame surface—this is attributed to rapid combustion. Visual observations of the flame show the flame central part as viewed from the *x*-direction (Fig. 4(d)) may rise and drop back to the deflection plate tips randomly. The flame fluctuates drastically a show significant turbulence. At Re_a = 445, such flame behavior is observed at the range 1376 < Re < 1806. At high a Reynolds number (Re = 2064) (Figs. 4(e) and (f)) the flame base is wide, takes a bowl shape, and shows distributed blue flame. The flame exhibits strong turbulence on its surface and is lifted, as can be observed from the *x*-direction view (Fig. 4 (f)), although it appears to be anchored on the deflection plates at one end probably due to end effect. At Re_a = 445, such flames were observed for the regime of Re > 1806. When Re_a was fixed at 445 it was observed that the flame becomes wider with a larger blue zone and displays stronger turbulence as the Reynolds number increases.

Fig. 5 shows typical flame images near the exit area of the burner at a co-flowing air rate of Re_a = 846. The flame images at low (Re = 344) and high (Re = 2064) Reynolds numbers in Fig. 5 correspond to those in Fig. 4. There is no correspondence

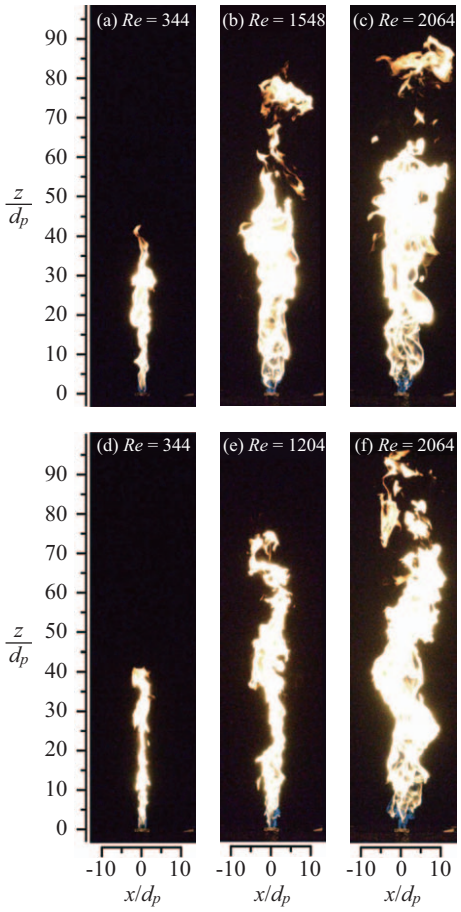

Fig. 6. Typical instantaneous full-length flame appearances of transversely-oscillating jet flame. Pictures taken with the camera facing the *y*-direction. Exposure time 1 ms. (a)-(c) Re_a = 445, (d) – (f) Re_a = 846.

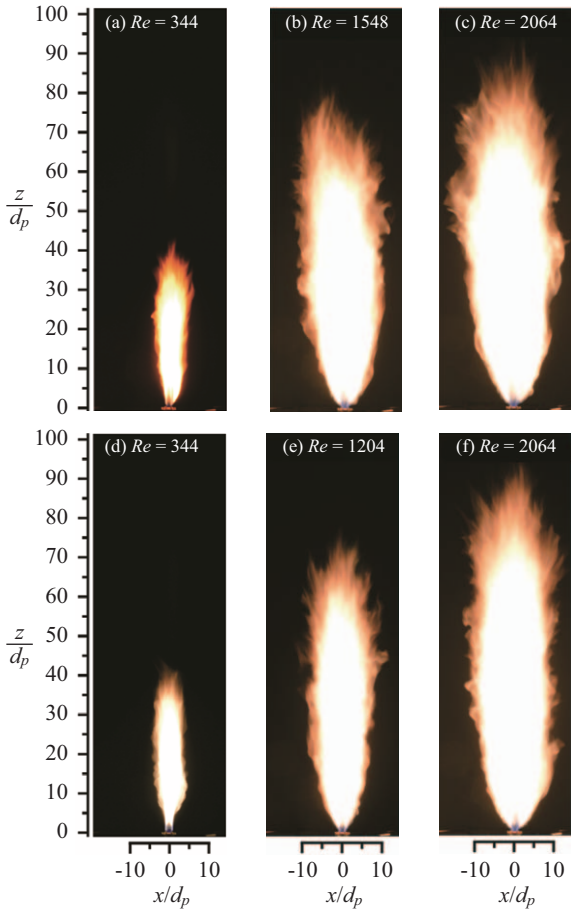

Fig. 7. Typical time averaged full-length flame appearances of transversely-oscillating jet flame. Pictures taken with the camera facing the *y*-direction. Exposure time 2 s. (a)-(c) Re_a = 445, (d)-(f) Re_a = 846.

for the mediate Reynolds numbers (Figs. 4(c) and (d), and Figs. 5(c) and (d)) because of the different transition points in the different co-flowing air. The images in Figs. 5(a), (c), and (e) were captured with the camera facing in the *y*-direction, while the images in Figs. 5(b), (d) and (f) were captured with the camera facing in the *x*-direction. At Re_a = 846 and at the range of fuel jet Reynolds numbers (*Re*) investigated, the flame remained attached. The flame images in Fig. 5 show stronger turbulence and appear to be narrower compared to the corresponding images in Fig. 4. Additionally, at *Re* = 2064 (Figs. 5(e) and (f)), the position of the lifted flame is not clear since the flame appear to at the beginning transition from attached to lifted. The images appear to be more wrinkled and burnt out when compared to Figs. 4(e) and (f). In Figs. 5(a), (c), and (e), the gap between the tips of the deflection plates appeared to be fully occupied by blue flames, which are unlike those shown in Figs. 4(a), (c), and (e) where the gap shows absence the of flames.

Comparing the flame images in Figs. 4 and 5 shows that the flame width decreases as the co-flowing air Reynolds number increases at the near exit area. Furthermore, the flame does not lift even though it appears more burned out when the co-flowing air Reynolds number is high. These results were viewed from the *x* direction (Figs. 4(f) and 5(f)). A higher co-flowing air Reynolds number seems to result in thinner flames with stronger turbulence. The width of the blue flame and the mix of blue and yellowish color in Figs. 4 and 5 indicate the role that transverse oscillations play in enhancing entrainment and mixing. When the Reynolds numbers for co-flowing air is higher, the flame may not lift in a higher fuel jet due to the effect of the deflection plates, which hold the flame. The photos in Figs. 4 and 5 show three flame modes that were identified in the literature (Huang et al., 2012; Yang et al., 2014a; Yang et al., 2014b): *attached flame*, *transitional flame*, and *lifted flame*. These modes correspond to Figs. 4(a) and (b), (c) and (d), and (e) and (f), respectively.

Fig. 6 presents the instantaneous full-length flame appearances, which correspond to Figs. 4 and 5. The images are captured with an exposure time of 1 ms with the camera facing in the *y*-direction. Figs. 6(a)-(c) show the flame images with co-flowing air of Re_a = 445, while Figs. 6(d)-(f) show flame images with co-flowing air of Re_a = 846. The flame images in Figs. 6(a)-(c) are wider compared to the corresponding flame images in Figs. 6(d)-(f). The flame image in Fig. 6(c) appears to be shorter when compared to the flame image in Fig. 6(f). The flame images in Figs. 6(d)-(f) have slightly longer blue flame zones compared

to the corresponding images in Figs. 6(a)-(c). In Fig. 6, it is clear that a higher co-flowing air Reynolds number (Re_a) results in thinner flames with higher blue lengths and stronger turbulence. The appearance of thinner flames with high co-flow air, Re_a, is attributed to the reduced rates of the jet spread and the decay of velocity due to constrained entrainment, which is the result of higher co-flow air stream momentum.

Figs. 7(a)-(f) show the typical long-exposure, full-length flame photographs that correspond to the short-exposure images shown in Figs. 6(a)-(f). Figs. 7(a)-(c) show flame photographs with co-flow air of Re_a = 445, whereas Figs. 7(d)-(f) show flame photographs at Re_a = 846. The photographs were taken with an exposure time of 2 s with the camera facing in the y-direction. The flame images in Figs. 7(a)-(c) appear to be wider than the corresponding photographs in Figs. 7(d)-(f). The flame images in Figs. 6(a)-(c) and Figs. 7(a)-(c) appear to occupy a larger area than the corresponding flame images in Figs. 6(d)-(f) and Figs. 7(d)-(f) respectively. The flame height and width increase as the Re increases with fixed co-flowing air, Re_a. However, the flame images appear to become shorter and thinner as the co-flowing air Reynolds number increases. It can be deduced that high co-flow Re_a may result in higher combustion rates, as observed in the smaller flame areas presented in Figs. 6(d)-(f) and 7(d)-(f).

3. Flame Modes Regimes

The characteristic flame modes observed in Figs. 4 and 5 are identified in the domain of Re and Re_a, as shown in Fig. 8. The bands of the short, slashed lines denote the borders between two different flame modes. The boundaries were identified by examining the actual flames and their corresponding images. Visual observations of the flame involved fixing the co-flow air Reynolds number (Re_a) at a constant value and then varying the fuel jet flow rate (Re), while in the meantime observing the occurrence of changes in the flame characteristics (as described in section 2). Visual and photographic observations of the flame were made both in the x- and y-directions in order to have a clear feature of the noticed trends in flame behavior. Three flame modes were identified: attached flame, transitional flame, and lifted flame. The attached flame remained anchored on the deflection plate tips all time with the flame showing smooth edges. At the transitional flame regime, visual observations of the flame and captured movies would show the flame exhibit random lifting and reattaching motion on the deflection plate tips. The borders separating the attached flame and the transitional flame regimes as well as the transitional flame and lifted flame regimes show an increasing trend as the co-flow air Reynolds number (Re_a) increases. For the instance at Re_a = 203 the lower and upper transition borders are at about Re = 1204 and 1462, respectively, and at Re_a = 445 the lower and upper transition borders would shift to Re = 1376 and 1806, respectively. Whereas at Re_a = 846 the lower and upper transition boundary appears at Re = 2150 and 2494, respectively. It is apparent that the transitional fuel jet Reynolds number becomes higher as Re_a increases. At a fixed Re_a at a particular

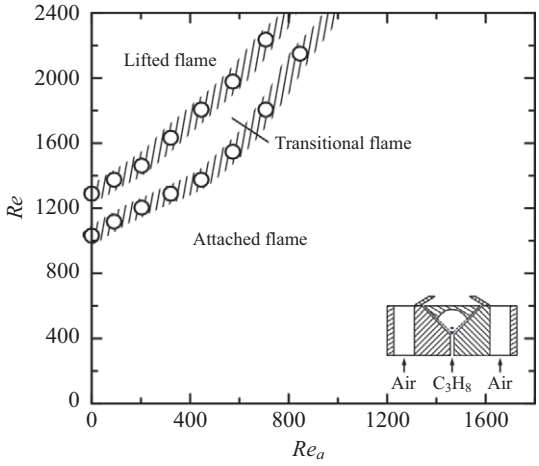

Fig. 8. Regimes of characteristic flame modes.

range of large Re, the visual observation and movies would see the flame remain lifted at an axial level of about $z > 0.8\ d_p$ away from the deflection plates, however, due to end effects at times the flame would anchor at the end tips of the plates interchangeably. The flames may remain attached at all fuel jet Reynolds numbers (Re) at extremely high co-flow air Reynolds numbers (Re_a). This is consistent with the observation that flames with high Re appear longer as Re_a increases. This implies that a flame with a larger co-flowing air Reynolds number may not lift easily off the burner compared to a flame with a smaller Re_a. This is attributed to the presence of the deflection plates.16

4. Flame Widths and Lengths

Fig. 9 shows dimensionless flame widths (W_f/d_p) at various co-flowing air Reynolds numbers (Re_a). Figs. 9(a), (c), and (e) present the flame widths as a function the dimensionless axial level (z/d_p). Figs. 9(b), (d), and (f) present the flame width as a function of the fuel jet Reynolds number (Re). In Figs. 9(a), (c), and (e), the flame width increases along with the axial distance to a maximum width and then, decreases. The width of a flame with a low Re_a value increases along with the axial distance at a faster rate than a flame with a high Re_a value. The flame widths shown in Figs. 9(a), (c), and (e) reveal the two major flame zones: the reaction zone, which exists as the lower flame portion (before the maximum width is reached) and the convection zone, which represents the upper flame portion (after the maximum width). The maximum flame width for a given Re decreases as the co-flowing air Re_a increases. The axial location of the maximum dimensionless flame width for the range $Re > 1204$ gets lower as the Re_a increases and is located within the axial range of $41 < z/d_p < 55$. When the Re ($Re < 1204$) value is low, the maximum flame widths are located within the axial range $14 < z/d_p < 34$, and the axial location decreases as Re_a increases. This is attributed to the delayed entrainment and mixing in the near-jet exit when the Re value in the fuel jet is high due to high axial momentum of the fuel and co-flow air

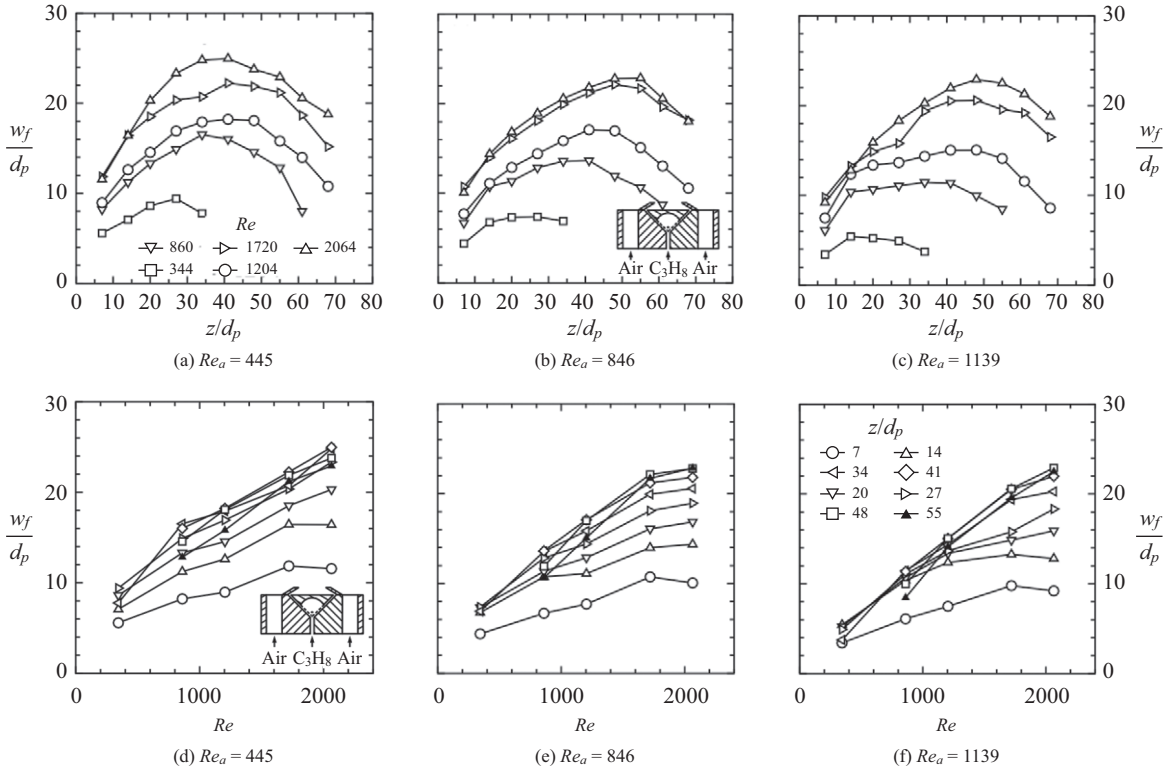

Fig. 9. Dimensionless flame widths at various fuel jet Reynolds numbers. (a), (b), and (c) flame widths at various *Re*, (d), (e), and (f) flame widths at various z/d_p.

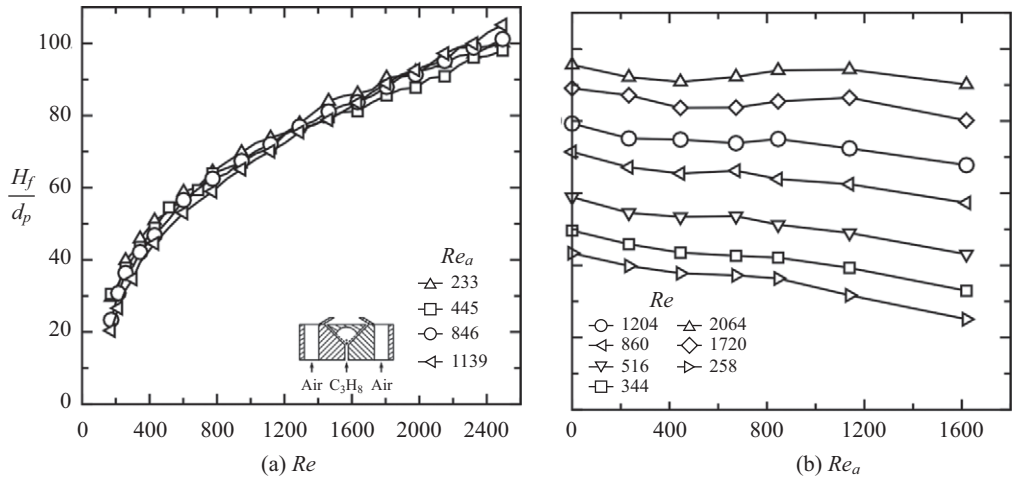

Fig. 10. Dimensionless flame lengths varying with (a) *Re*, (b) Re_a.

jets. When the co-flowing air is $Re_a = 445$, the maximum flame width at $Re = 2064$ may be approximately $W_f/d_p = 25$ and it may occur at the axial level of approximately $z = 41d_p$. However, when the co-flow air is $Re_a = 846$, the maximum flame width at $Re = 2064$ may be approximately $W_f/d_p = 22.9$ at the axial level of approximately $W_f/d_p = 54.5$. Figs. 9(b), (d) and (f) show the flame width as a function of *Re* at fixed axial levels. The dimensionless flame widths, W_f/d_p, increase linearly as *Re* increases. When *Re* is low, the flame widths almost merge at one location in high co-flowing air Re_a, which is an indicator of a flame with a nearly constant width. The maximum dimensionless flame widths (W_f/d_p) for $Re = 344$ flames are 9.4 and 7.4 at $Re_a = 445$ and $Re_a = 846$, respectively.

Fig. 10 presents the dimensionless flame lengths (H_f/d_p) of the transversely oscillating plane jet flames with various co-flowing air (Re_a). The dimensionless flame lengths (H_f/d_p) increased as Re increased. In the region $Re < 1204$, the flame lengths for all of the co-flowing air (Re_a) increased rapidly as

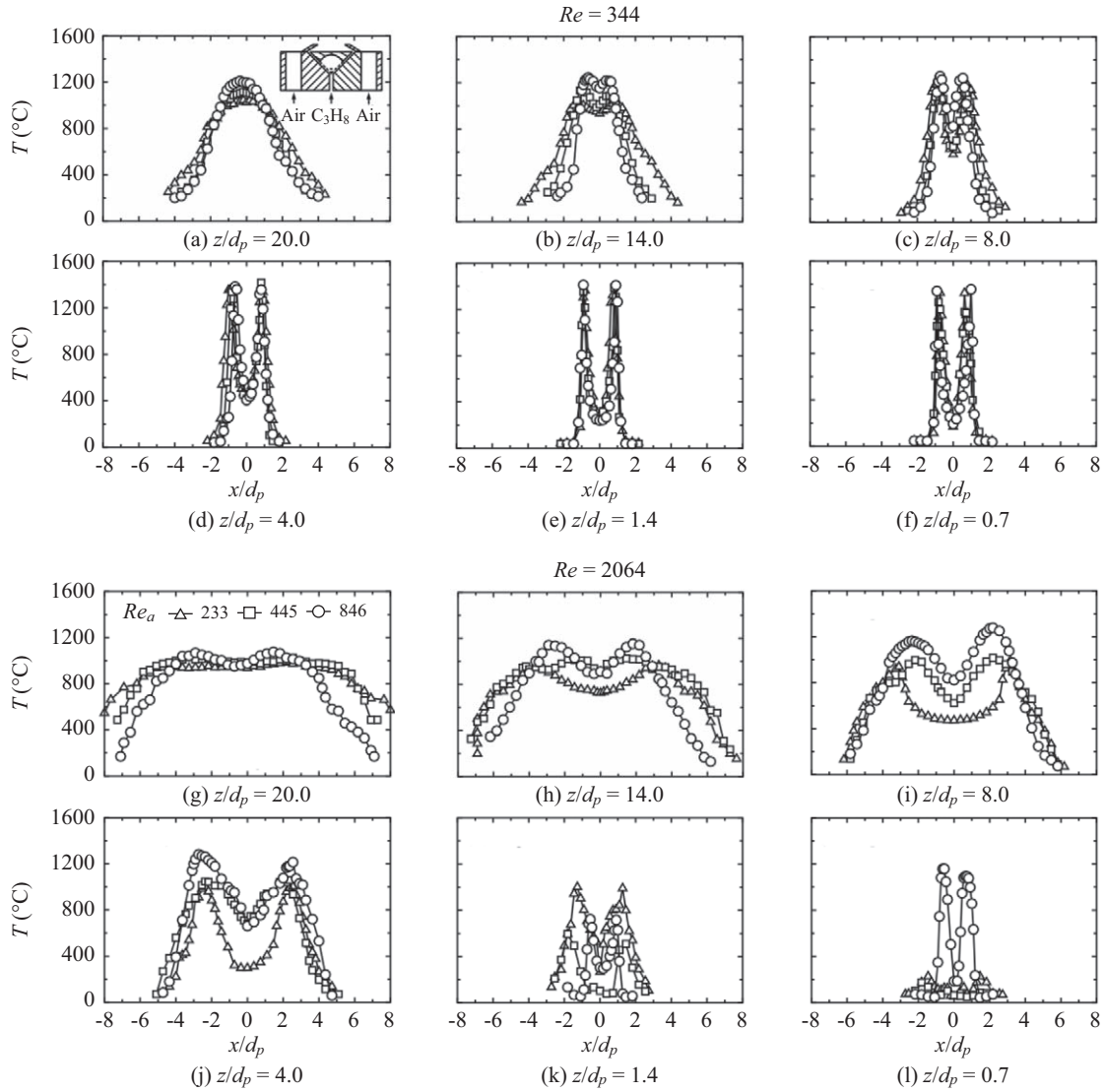

Fig. 11. Transverse temperature distributions of transversely-oscillating jet flames at various axial altitudes. (a)-(f) attached flame *Re* = 344, (g)-(l) lifted flame *Re* = 2064.

Re increased. In the region *Re* > 1204, the flame lengths also increased as *Re* increased, but at slower rates. The flame lengths decreased as the co-flowing air Reynolds number increased, as shown in Figs. 10(a) and (b). However, when the fuel jet Reynolds number (*Re*) was higher than approximately 1400 for a fixed *Re*, the dimensionless flame lengths (H_f/d_p) increased slightly as Re_a increased. In the region *Re* > 1400, Re_a = 445 exhibits shorter flames compared with the other cases of co-flowing air investigated. Meanwhile, in the region *Re* < 1400, Re_a = 1139 produced shorter flames. With co-flowing air of Re_a = 445, the dimensionless flame length (H_f/d_p) may have changed from approximately 43.5 at *Re* = 344 to approximately 90.4 at *Re* = 2064. With co-flowing air of Re_a = 846, the dimensionless flame lengths (H_f/d_p) change from approximately 42.1 at *Re* = 344 to approximately 94.1, at *Re* = 2064. These observations indicate that co-flowing air improves the combustion rate by enhancing entrainment and mixing. However, extend of enhancing the combustion process is dependent on the selected combination of fuel and co-flowing air jets. Combining jets with high axial momentum may result in longer flames due to constrained entrainment at the jet interfaces. The similar flame lengths for different co-flowing is attributed to the transverse oscillation of the fuel jet, which promotes entrainment even with high jet momentum.

5. Temperature Distributions

Fig. 11 shows the transverse temperature distributions. The Reynolds numbers of the co-flowing air (Re_a) are 233, 445, and 846 and the Reynolds numbers of the fuel jet (*Re*) are 344 and 2064. At low fuel jet Reynolds number *Re* = 344 and at low axial levels (z/d_p < 14), the temperature profiles present two peaks with central dips, which are the characteristics of diffusion

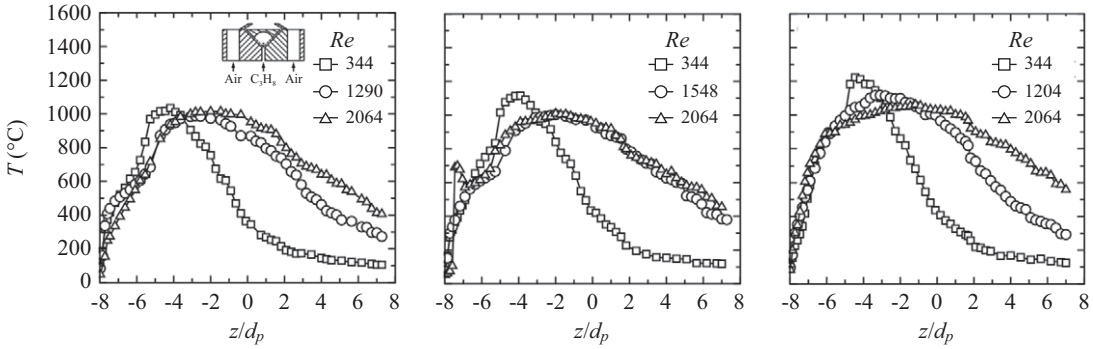

Fig. 12. Temperature distributions along central axis of transversely-oscillating jet flame at various *Re*. (a) Re_a = 233, (b) Re_a = 445, (c) Re_a = 846.

flames (Figs. 11(a)-(f)). However, at high axial levels (z/d_p > 14), the temperature distributions turn Gaussian. This corresponds to the maximum flame widths shown in Fig. 9. The maximum flame temperatures at a fixed axial level increases as the co-flowing air (Re_a) increases. Maximum temperatures of approximately 1035°C, 1115°C, and 1220°C are attained when the Reynolds numbers of co-flowing air are Re_a = 233, 445, and 846, respectively.

Figs. 11(g)-(l) show the temperature distributions at high fuel jet Reynolds number (*Re* = 2064) at various axial levels for co-flowing air at Re_a = 233, 445, and 846. At low axial levels (z/d_p < 14), the temperature distributions show twin-peak profiles with central dips. These temperature profiles exhibit features of diffusion flames. In the region $z/d_p \geq 4$, the central-temperatures increase as the axial level (z/d_p) increases. Meanwhile, the peak values standing at the two sides decrease slightly as z/d_p increases. The temperature distributions take the form of plateaus at high axial levels (z/d_p > 14). The temperatures at the axial levels ($z/d_p \leq 1.4$) are low or even indicate lack combustion because this region lies at the section between the burner top and the lifted flame, which is a pre-mixed region. The temperature distributions widen as the z/d_p value increases. At an axial level of approximately z/d_p = 20, the temperature profiles with co-flowing air of Re_a = 233 and Re_a = 445 show no central dips. Meanwhile, the temperature distribution at Re_a = 846 shows a shallow central dip, which indicates that the flame is not yet fully combined. These findings correspond to Fig. 10 where the flame lengths with high *Re* values are observed to increase as Re_a increases, thus indicating that for a combination of high *Re* and high Re_a combustion delays due to high momentum possessed by the jets. The co-flowing air with a value of Re_a = 846 presents a slightly narrower temperature distribution, which indicates a narrower flame as noted in Fig. 9. The peak temperature values increase as the Re_a value increases. At *Re* = 2064, the flames attain maximum temperatures of approximately 1005°C, 1060°C, and 1280°C when the co-flowing air is Re_a = 233, 445, and 846, respectively. These findings on transverse temperature distributions explain the effects that the strength of co-flowing air may have when combusting a transversely oscillating fuel jet: i.e., a rapid combustion process that occurs due to increased entrainment and mixing processes.

Figs. 12(a)-(c) show flame temperature distributions along the central axis with various fuel jet Reynolds number when the co-flowing air is Re_a = 233, 445, and 846, respectively. The central axis flame temperatures increase rapidly as the axial level (z/d_p) increases. They also attain a maximum value and then decrease in the high-level flame region. When the fuel jet Reynolds number is *Re* = 344, the peak temperature appears at a lower flame level, compared to the maximum temperatures in flames with mediate and high Re values. At *Re* = 344, the flames attain maximum central axis temperatures of about 1035°C (at $z/d_p \approx 19$), 1115°C (at $z/d_p \approx 20.5$), and 1220°C (at $z/d_p \approx 17.7$) for Re_a = 233, Re_a = 445, and Re_a = 846, respectively. When the fuel jet is high, the flames with Reynolds number of *Re* = 2064 attain maximum central axis temperatures of 1015°C, 1010°C, and 1060°C appearing at an axial level of $z/d_p \approx 32.7$, for co-flowing air at Re_a = 233, 445, and 846, respectively. The values of the maximum central temperature increased as Re_a increased, and were particularly high when the *Re* value was low. The high co-flowing air (Re_a) plots in Figs. 12(a)-(c) show narrower peaks, smaller reaction zones, and smaller convection zones compared with low Re_a plots. This implies that high coflowing air may result in higher mixing and reaction rates, thus leading to a complete combustion process.

6. Product Concentration Distributions

Fig. 13 show the combustion product concentrations of the transversely oscillating plane jet flame at *Re* = 2064. The co-flowing air is Re_a = 445. Figs. 13(a) and 13(b) show that, the CO_2 and CO concentrations of z/d_p = 0.7 and z/d_p = 1.4 are almost zero. This corresponds to the temperature profiles shown in Figs. 11(k) and 11(l), which indicate a region with no combustion-due to the existence of a lifted flame. In the region z/d_p < 14, the CO_2 and CO concentrations profiles present a twin-peak distribution with low central values, which indicates that the combustion region is not yet fully merged. These are features of a diffusion flame. However, at z/d_p = 20, the CO_2 and CO concentration profiles nearly plateau distributions, revealing a nearly fully combined combustion zone. The central region values of both the CO_2 and CO concentrations increased

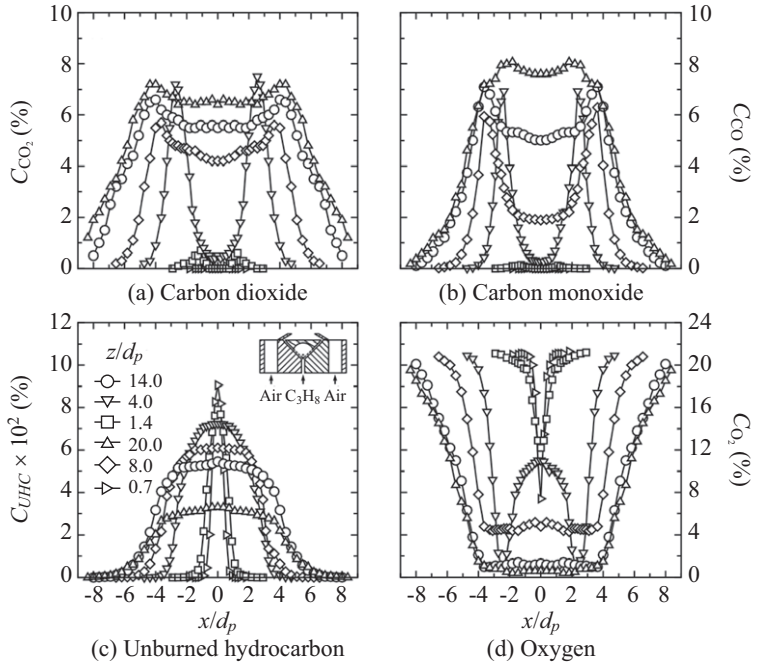

Fig. 13. Combustion product concentration distributions of transversely-oscillating jet flame at Re_a = 445 and various axial altitudes. Re = 2064.

along with the axial level (z/d_p). In Figs. 13(a) and 13(b), the maximum CO_2 and CO concentration values are approximately 7.2% and 8.1%, respectively, at $z/d_p = 20$. As shown in Fig. 13(c), the unburned hydrocarbon concentrations (C_{UHC}) spread wider as the axial level (z/d_p) increases. However, the central peak value decreased rapidly as the z/d_p value increased. The distribution of the unburned hydrocarbon took the form of a plateau, which showed the ability of the transversely oscillated plane jet to entrain and mix. The unburned hydrocarbon concentrations attained a maximum value of approximately 9.1% at level of $z/d_p = 0.7$ on the central axis. However, at the level $z/d_p = 20$ it registered a maximum value of approximately 3.3%. Fig. 13(d) shows the oxygen (O_2) concentrations at Re = 2064 and Re_a = 445. At lower levels ($z/d_p < 1.4$), the O_2 concentration distributions show typical profiles of a diffusion flame. However, in the region $z/d_p > 8$, the O_2 concentration distributions indicate a premixed flame. The O_2 diffuses from the environment toward the flame zone and is consumed in the reaction zone. Under normal circumstances, the O_2 would not be expected to diffuse to the central axis of the flame because it is consumed as it diffuses. However, as shown in Fig. 13(d), the oxygen concentration appeared at lower levels ($z/d_p = 0.7$, $z/d_p = 1.4$, $z/d_p = 4$). For example, the oxygen concentration is 7.4% at $z/d_p = 0.7$ along the central axis. At higher levels, the oxygen concentration does not reach zero inside the flame, as expected. Instead, there is still oxygen concentrations at the central axis of about 0.4% at $z/d_p = 20$. The product concentration distributions revealed the effects of the transversely oscillated plane fuel jet when entrainment and mixing were enhanced, which may have caused the combustion to be faster and more efficient.

IV. CONCLUSIONS

The flame behaviors and thermal structure of transversely oscillating plane jet flames were studied using a V-shaped fluidic-oscillator burner with deflection plates installed at 60 degrees to vertical. The transversely oscillating fuel jet emerged in an environment of co-flowing air that was supplied from rectangular channels on the parallel sides of the burner. The impacts of the co-flowing air on flame behavior and thermal structure were assessed by varying the co-flowing air Reynolds number. The following conclusions were drawn from the results:

(1) The installation of deflection plates in a V-shaped fluidic-oscillator induced transverse oscillations in the alternately pulsating issued jets. The frequency of the periodic transverse oscillations increased linearly as the supply jet velocity increased. The Strouhal number of the transversely oscillating jet may attain an asymptotic value of approximately 0.188 with an airflow Reynolds number of approximately 230.

(2) At the near burner exit region, the flame base showed distributed blue color with strong turbulence. This was attributed to the transversely oscillating jet that enhanced the entrainment and mixing of the fuel jet and the co-flowing air jets. From the near exit region, three flame modes were observed in the domain of Re and Re_a: attached flame, transitional flame, and lifted flame. The flames remained attached when the Re_a value was greater than approximately 1000.

(3) With fixed co-flowing air, the flame widened showing larger blue zones and stronger turbulence as the fuel jet Reynolds number increased. Meanwhile, the flame with the fixed

fuel jet appeared to become shorter and thinner as the co-flowing air Reynolds number increased. This is because the rate of the jet spread and the velocity decay were reduced due to the constrained entrainment, which resulted from the high momentum of the co-flowing jets.

(4) The flame widths and lengths in the fixed co-flow air increased linearly as the fuel jet velocity increased. The maximum flame width decreased as the co-flowing air and the Reynolds number (Re_a) increased. The axial location of the maximum flame width in the $Re < 1204$ region of fuel jet flow became lower as the co-flowing air (Re_a) increased. However, at the-region $Re > 1204$, the axial location of the maximum flame width increased along with Re_a for a fixed Re. Additionally, in the region $Re < 1400$ the flame lengths decreased as the co-flowing air Reynolds number (Re_a) increased. However, in the region $Re > 1400$, the flame lengths increased slightly as Re_a increased.

(5) The transverse temperature distributions with flame axial levels of $z/d_p < 14$ were two-peaked with central dips that became shallower as the axial flame level increased. However, at flame axial levels of $z/d_p > 14$, the temperature profiles turned into Gaussian distributions with plateaus that appeared in when the fuel jet Reynolds numbers were high. When the fuel jet Reynolds number was $Re = 2064$, the flames produced with high co-flowing air of $Re_a = 846$ attained maximum temperatures of approximately 1280°C. Meanwhile, the maximum temperature of the flame produced at a lower co-flow of $Re_a = 445$ was approximately 1060°C. The axial temperature distributions divided the flame into two regions, a reaction zone and a convection zone, which were separated by maximum (peak) values. The maximum flame axial temperatures became higher as the co-flowing air Reynolds number increased. Furthermore, the higher coflowing air ($Re_a = 846$) created higher axial temperatures by–approximately 100°C compared to the lower co-flowing air (Re_a).

Overall, a transversely oscillating jet resulted in a wide blue flame base with strong turbulence due to enhanced entrainment and mixing. A higher co-flowing air environment improved the combustion rate, especially with moderate fuel jet Reynolds numbers. However, the extent to which the co-flowing air enhanced combustion depended on the supplied combination of fuel and the velocities of the co-flow coflow air jet.

V. NOMENCLATURE

AR	aspect ratio of rectangular channel
b	width of exit slots of fluidic oscillator, 0.5 mm
b_t	coflow channel plate thickness, 2 mm
D	channel width of co-flowing air, 5.5 mm
d	width of fluidic oscillator channel, 1 mm
d_p	separation distance between deflection plates tips, 11 mm
h	offset distance from crescent origin to virtual vertex of target blockage, 2 mm
H_f	flame length
l	length of deflection plates, 5.5 mm
Q_a	volumetric flow rate of co-flowing air jet measured by rotameter
Q	volumetric flow rate of fluid jet measured by rotameter
R	radius of crescent profile of the target blockage, 4.5 mm
Re_a	Reynolds number of coflow air jet flow, u_aD/v_a
Re	Reynolds number of fuel jet flow, u_jd_p/v_j
s	span length of burners, 36 mm
St	Stroual number of jet oscillations, fd_p/u_j
T	temperature, °C
u	instantaneous jet velocity, m/s
u_a	average exit velocity of coflowing jet, $Q_a/(sD)$
u_j	average exit velocity of plane jet, $Q_j/(sd)$
w	overall width of V-shaped fluidic-oscillator burner, 36 mm
w_b	downstream width of target blockage, 15 mm
W_f	flame width
x, y, z	coordinates in lateral, span, and axial directions fixed at centre of burner exit plane
θ	deflection angle of deflection plates measured from vertical axis, 60 degrees
v_a	kinematic viscosity of air
v_j	kinematic viscosity of fuel jet

REFERENCES

Akbarzadeh, M. and M. Birouk (2014). Liftoff of a co-flowing non-premixed turbulent methane flame: Effect of the fuel nozzle orifice geometry. Flow Turbulence Combust 92, 903-929.

Boucher, R. F. and C. Mazharoglu (1988). Low reynolds number fluidic flow-metering. Journal of Physics E: Scientific Instruments 21, 977-989.

Brown, C. D., K. A. Watson and K. M. Lyons (1999). Studies on lifted jet flames in coflow: The stabilization mechanism in the near- and far-fields. Flow, Turbulence and Combustion 62, 249-273.

Chang, K.T. and R. F. Huang (2004). Development and characterization of jet-injected vee-gutter. Journal of Mechanics 20, 77-83.

Chen, C.-K., L. Wang, J.-T. Yang and L.T. Chen (2006). Experimental and computational analysis of periodic flow structure in oscillatory gas flow meters. Journal of Mechanics 22, 137-144.

Del Campo, D., J. M. Bergada, V. Del Campo (2015). Preliminary study on fluidic actuators. Design modifications., in: Mastorakis, N. E., Rudas, I., Shitikova, M. V., Shmaliy, Y. S. (Eds.), International Conference on Mechanics, Materials, Mechanical Engineering and Chemical Engineering, Barcelona, Spain, 53-61.

Deo, R. C., J. Mi and G. J. Nathan (2007). The influence of nozzle aspect ratio on plane jets. Experimental Thermal and Fluid Science 31, 825-838.

Gebhard, U., H. Hein and U. Schmidt (1996). Numerical investigation of fluidic micro-oscillators. Journal of Micromechanics and Microengineering 6, 115-117.

Gregory, J. W., J. P. Sullivan, G. Raman and S. Raghu (2007). Characterization of the microfluidic oscillator. AIAA Journal 45, 568-576.

Huang, R. F. and K. T. Chang (2005). Fluidic oscillation influences on v-shaped bluffbody flow. AIAA Journal 43, 2319-2328.

Huang, R.F. and K.T. Chang (2007). Evolution and turbulence properties of self-sustained transversely oscillating flow induced by fluidic oscillator. Journal of Fluids Engineering 129, 1038.

Huang, R. F., H. F. Yang and C. M. Hsu (2012). Flame behavior and thermal structure of combusting nonpulsating and pulsating plane jets. Journal of Propulsion and Power 29, 114-124.

Joyce, J. W. (1983). Fluidics: Basic components and applications. US Army Electronics Development Command, Harry Diamond Labs Special Re-

port HDL-SR-83-9,
Mack, M., R. Niehuis and A. Fiala (2011). Parametric study of fluidic oscillators for use in active boundary layer control. ASME Paper No. GT2011-45073.
Mataoui, A. and R. Schiestel (2009). Unsteady phenomena of an oscillating turbulent jet flow inside a cavity: Effect of aspect ratio. Journal of Fluids and Structures 25, 60-79.
Mi, J. and G. J. Nathan (2005). Statistical analysis of the velocity field in a mechanical precessing jet flow. Physics of Fluids 17, 1-17.
Montgomery, C. J., C. R. Kaplan and E. S. Oran (1998). The effect of coflow velocity on a lifted methane-air jet diffusion flame. Twenty-Seventh Symposium (International) on Combustion 27, 1175-1182.
Namazian, Z. (2016). Effect of velocity on the length of flames in turbulent nonpremixed flames. International Journal of Mechanical And Production Engineering 4, 9-12.
Olivotto, C. (2010). Fluidic elements based on coanda effect. Incas Bulletin 2, 163-172.
Raghu, S. (2013). Fluidic oscillators for flow control. Exp Fluids, 1-11.
Rasheed, F. (2013). Development of fluidic oscillator based active flow control system for wind turbine blades. The Eighth Asia-Pacific Conference on Wind Engineering APCWE-VIII, 1286-1293.
Shakouchi, T. (1989). A new fluidic oscillator, flowmeter, without control port and feedback loop. Journal of Dynamic Systems, Measurement, and Control 111, 535-539.
Sun, C.-L. and C.-Y. Sun (2011). Effective mixing in a microfluidic oscillator using an impinging jet on a concave surface. Microsyst Technol 17, 911-922.
Tesař, V., E. Smyk and K. Peszynski (2014). Fluidic oscillator with bistable turn-down amplifier. Colloquium Fluid Dynamics 2014 1-14.
Tesař, V., S. Zhong and F. Rasheed (2013). New fluidic-oscillator concept for flow-separation control. AIAA Journal 51, 397-405.
Uzol, O. and C. Camci (2002). Experimental and computational visualization and frequency measurements of the jet oscillation inside a fluidic oscillator. Journal of Visualization 5, 263-272.
Yang, H. F., C. M. Hsu and R. F. Huang (2014a). Controlling plane-jet flame by a fluidic oscillation technique. Journal of Engineering for Gas Turbines and Power 136, 1-10.
Yang, H. F., C. M. Hsu and R. F. Huang (2014b). Flame behavior of bifurcated jets in a v-shaped bluff-body burner. Journal of Marine Science and Technology 22, 606-611.
Yang, J.-T., C.-K. Chen, I.-C. Hu and P.-C. Lyu (2007a). Design of a self-flapping microfluidic oscillator and diagnosis with fluorescence methods. Journal of Microelectromechanical Systems 16, 826-835.
Yang, J.-T., C.-K. Chen, K.-J. Tsai, W.-Z. Lin and H.-J. Sheen (2007b). A novel fluidic oscillator incorporating step-shaped attachment walls. Sensors and Actuators A 135, 476-483.